Measuring Color Defects in Flat Panel Displays using HDR Imaging and Appearance Modeling

Giljoo Nam, Haebom Lee, Sungsoo Oh, Min H. Kim, *Member, IEEE*

Abstract—Measuring and quantifying color defects in flat panel displays (FPDs) are critical in the FPD industry and related business. Color defects are traditionally investigated by professional human assessors as color defects are subtle perceptual phenomena that are difficult to detect using a camera system. However, human-based inspection has hindered the quantitative analysis of such color defects. Thus, the industrial automation of color defect measurement in FPDs has been severely limited even by leading manufacturers accordingly. This paper presents a systematic framework for the measurement and numerical evaluation of color defects. Our framework exploits high-dynamic-range (HDR) imaging to robustly measure physically-meaningful quantities of subtle color defects. In addition to the application of advanced imaging technology, an image appearance model is employed to predict the human visual perception of color defects as human assessors do. This proposed automated framework can output quantitative analysis of the color defects. This work demonstrates the performance of the proposed workflow in investigating subtle color defects in FPDs with a high accuracy.

Keywords—*flat panel display, LCD, mura, color defect, inspection, high-dynamic-range imaging, image appearance model.*

I. INTRODUCTION

VISION-based measurement (VBM) has been utilized to detect defected products automatically in manufacturing processes [1]. Many VBM systems have been proposed for diverse product types, such as glass [2], rubber profile [3] and weld bead [4].

Various defects occur in a flat panel display (FPD) during the production and assembly of FPDs. The types of defects can be classified into two categories: achromatic and chromatic defects. Achromatic defects in FPDs are so-called *mura* defects. A number of methods for automatic mura detection have been proposed [5]–[10], and some manufacturers have adopted these systems to reduce production costs and enhance production quality. However, mura detection methods only consider the variance of *luminance* in FPDs and are incapable of detecting chromatic defects in displays. Perceptually meaningful investigation of chromatic defects in FPDs has rarely been discussed.

A chromatic defect, or a color defect, is defined as an abnormal reproduction of colors or perceivable regional color variations in a display. The most common color defect in FPDs is a yellow tint in the screen. There are several causes of such color defects. For instance, adhesive materials, which are

Giljoo Nam, Haebom Lee and Min H. Kim are with KAIST School of Computing, Korea (corresponding author's e-mail: minhkim@kaist.ac.kr). Sungsoo Oh is with the Production Engineering Research Institute of LG Electronics. Manuscript received April 10, 2015; revised August 5, 2015.
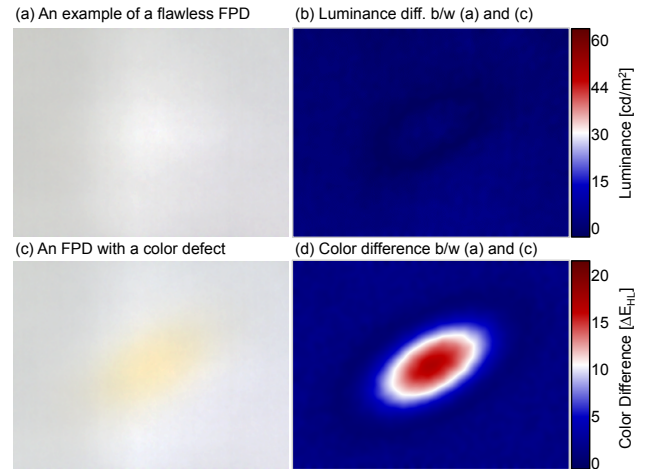

Fig. 1: While traditional investigations of FPD defects only account for luminance variation, our proposed workflow investigates FPD color defects with physically-meaningful imaging and image appearance modeling that quantifies the perceived color defects. (a) and (c) show a flawless and a faulty display. (b) compares luminance difference between (a) and (c), which is a common metric used in the FPD industry. This error map is incapable of distinguishing them. (d) compares the difference using our workflow, distinguishing the fault one effectively although the color difference is subtle.

used to bond optical components and transparent films, may become brown or yellow during UV curing. Color variation also occurs across the screen when a color filter array inside a TFT-LCD panel is not manufactured uniformly. Furthermore, flaws in component assembly also generate color variation. For example, a screw that is too strongly tightened along an edge can cause a yellow region to appear near the edge. In fact, color defects are inevitable in the FPD manufacturing process.

In assembly lines, human assessors are traditionally hired to detect color defects in FPDs. Setting aside the slow and costly aspect of manual inspection, there is a fundamental limitation. Color is psychological perception although it is triggered by physical radiation. Therefore, there is no guarantee that the colors perceived by different workers are the same. Eye fatigue, viewing conditions, adaptation, personal experience, and even culture may affect the human perception of colors [11], [12]. In other words, the performance of color defect inspection in FPDs depends on the visual perception of the workers, which varies from person to person. Thus, it is necessary to quantify such colorimetric measurements systematically and define color defects in terms of human visual perception for FPD inspection.

To this end, this paper presents a systematic framework for detecting color defects in FPDs. Figure 1 illustrates the necessity of the proposed color difference-based inspection method against a luminance-based inspection method. This proposed method does not depend on type or size of FPDs. The contributions of this paper are:

- A novel automated workflow to inspect color defects in FPDs as human assessors do,
- The application of high-dynamic-range (HDR) imaging for physically-meaningful measurements of the radiometric quantity of light in FPDs, and
- The application of an image appearance model for perceptually uniform metrics of color defects in FPDs that accounts for the contrast sensitivity of the human visual system (HVS).

II. BACKGROUND AND RELATED WORK

A. Measuring Flat Panel Displays

Semiconductor Equipment and Materials International (SEMI) [13] standardized a just noticeable difference (JND) on *mura*, in terms of luminance contrast and defect area. The SEMI JND is currently widely used for most FPD mura detection research [6], [7]. Although the standard successfully defines and quantifies the monochromatic defects in FPDs in terms of *luminance*, it disregards regional *color* defects and associated measurement protocols. In contrast, this proposed method numerically evaluates any color defects with perceptually meaningful metrics.

1) Mura Detection: Many types of mura defects in FPDs, such as line-type mura, bright/dark region mura, and light leaking on the edges, appear with a certain level of high frequency. Various methods have been proposed to filter out these high frequency errors from low frequency background using a level-set technique [6], low-pass filtering [14], linear regression models [8], and discrete cosine transform [7]. Recently, Gan and Zhao [9] proposed an active contour model for detecting mura in FPDs. They modified a contour detection method to make their method robust to initial contour guesses and suitable for finding subtle mura boundaries. However, these mura detection methods have been limited to investigating luminance variation. Therefore, these methods are unsuitable for detecting color defects as shown in Figure 1.

2) Color Defect Detection: Detecting color defects in FPDs has rarely been discussed in contrast to mura detection. Son et al. [15] presented a method for detecting a small color defect region by measuring the difference between the diffraction patterns of two incident pixels with a line scan camera. Asano et al. [16] presented systems for inspecting color uniformity over the entire screen. Their methods focused on measuring screen uniformity in RGB channels respectively, while disregarding human color perception.

These previous work disregard the perceptual aspect of color defects. Recently, Asano et al. [17] proposed a seminal approach that numerically quantizes color defects using a spatially-varying color space, S-CIELAB [18]. However, they did not explicitly propose how to measure color defects and how to detect a color-defected region in an FPD. Furthermore, the employed color difference metric was ΔE_{ab}^*, which was built in 1976, and it is perceptually less uniform than the state-of-the-art color difference models [19].

B. HDR Imaging

High-dynamic-range (HDR) imaging has been used to overcome the limited range of captured radiance in an ordinary camera [20], [21]. HDR imaging also enables dense radiance sampling on each point, thus yielding a higher signal-to-noise ratio [22]. Modern display technology allows for an LCD display with a high contrast ratio of more than 1:16,384 ($=2^{14}$), which exceeds the dynamic range of an ordinary camera of a 12- or 14-bit ADC. HDR imaging is a great alternative for investigating advanced display products. Kim and Kautz [23] proposed a camera characterization method for HDR imaging and showed that the HDR characterization method yields physically accurate measurement of colors. This paper exploits this HDR characterization method that converts the device-dependent HDR RGB signals to device-independent color coordinates of CIEXYZ. This application of HDR imaging allows us to detect any subtle color defects in FPDs as a radiance map in absolute scales with high accuracy. In addition, once the HDR imager is characterized, it can measure absolute radiance regardless of the luminance level of the target FPD.

C. Image Appearance Models

Color appearance models have been used to represent colors in perceptually-uniform coordinates in a vector space, where the Euclidean distance between two colors presents the perceived difference between the two colors [11], [12]. These color appearance models quantify colors in points, whereas image appearance models are used to predict perceived color appearance in an image, accounting for the spatial context of surrounding colors with respect to the frequency of color differences. Zhang and Wandell [18] introduced a spatial extension of the CIELAB color space, so-called S-CIELAB, which is an image appearance model with contrast sensitivity functions (CSFs). Fairchild and Johnson [24] presented an image appearance framework, so-called iCAM, for image quality assessment. Wang et al. [25] introduced a multiscale framework for image quality assessment, so-called structural similarity (SSIM). Lissner et al. [26] extended the idea of SSIM to color images. In their framework, they used a perceptually-uniform color space, called LAB2000HL [19], where the color space builds on the revised color difference formulae of CIE DE2000. The Euclidean distance in this coordinates improves perceptual uniformity in evaluating color differences. This proposed framework chooses the LAB2000HL space [19] as the main color space and adopts the contrast sensitivity functions in the iCAM framework [24], following Lissner et al. [26].

III. PROPOSED FRAMEWORK

A. Overview

First, a commodity machine vision camera is characterized and ready to be used as a 2D colorimeter via HDR imaging
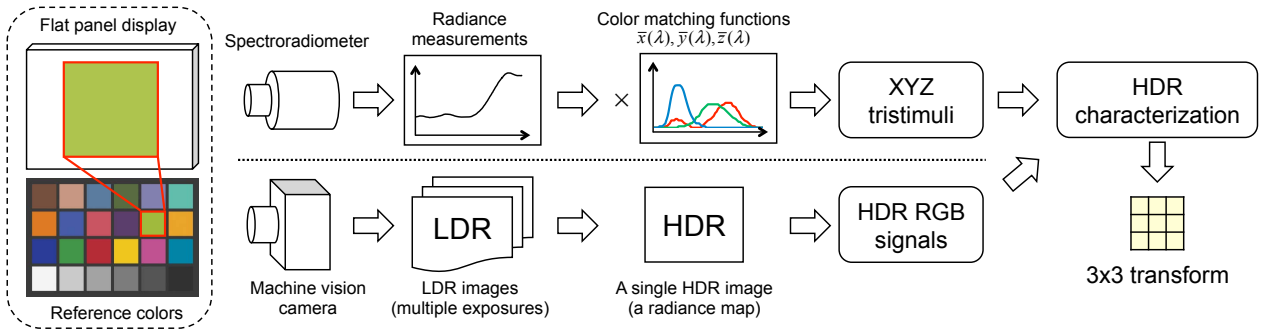
Fig. 2: Overview of our calibration protocol (see Section III-B) for HDR imaging [23], allowing for measuring radiometric quantities in an FPD. Each color patch in a target, a Digital ColorChecker, is displayed in an FPD. The 24 color patches are captured sequentially with both a spectroradiometer and a camera. This HDR characterization yields a linear transformation that converts RGB camera signals into CIEXYZ values, enabling physically-meaningful measurements of colors like a spectroradiometer.

(see Section III-B). Second, a flawless FPD is selected as a reference display. It is used as a base FPD to be compared with test target devices (Section III-C). Third, the captured color radiance maps of both reference and test FPDs are then mapped into color coordinates in an image appearance model (Section III-D). This appearance model allows for perception-based quality inspection. Lastly, a color difference map is calculated by comparing the perceptual coordinates of the reference and the test FPDs (Section III-E). This map records perceptual color differences in the test FPD with regard to the reference FPD, and it is utilized to identify faulty products.

B. HDR Characterization

Each color patch in a color target, a Digital ColorChecker, shown on the left-hand side of Figure 2, is displayed sequentially on an FPD. The 24 color patches are captured with both a calibrated spectroradiometer and a machine vision camera simultaneously. The camera captures multiple images with different exposures and the images are combined into an HDR image. An HDR radiance map is reconstructed as follows:

$$L = \left\{ \sum_{k=1}^{N} \omega(X_k) X_k \right\} \bigg/ \left\{ \sum_{k=1}^{N} \omega(X_k) \right\}, \quad (1)$$

where L is the reconstructed HDR radiance map, X_k is the LDR image under exposure k, N is the number of different exposures, and $\omega()$ is a trapezoidal weighting function that accounts for noise and saturation in input LDR images.

The spectral power distribution of the color patch, measured by the spectroradiometer, is converted into CIEXYZ tristimulus values using the CIE color matching functions of $\bar{x}(\lambda)$, $\bar{y}(\lambda)$ and $\bar{z}(\lambda)$. Using the 24 pairs of the HDR RGB signals and the CIEXYZ tristimulus values, the HDR characterization process optimizes a linear problem to yield a 3×3 linear matrix M:

$$M = (A^\top A)^{-1} A^\top B, \quad (2)$$

where $A \in \mathbb{R}^{24\times3}$ is a matrix of HDR RGB signals and $B \in \mathbb{R}^{24\times3}$ is a matrix of XYZ tristimulus values. This matrix M allows us to obtain radiance levels in FPDs as XYZ tristimulus values B' by multiplying new HDR RGB signals A' with the calibration matrix M: $B' = A'M$. In particular, this HDR

characterization method [23] yields the absolute radiance values of color measurements in FPDs in absolute scales. We can measure the luminance intensity per pixel in FPDs [unit: cd/m^2] as the Y channel, i.e., this protocol makes the employed RGB camera function as a 2D spectroradiometer. See Section V-A for the accuracy of our characterization method.

C. Reference Display

Our objective is to detect visible color defects which can be perceived distinctively with respect to properly finished FPD products. To this end, a reference image (calibrated in CIEXYZ) of a well finished FPD product is captured, which includes the spatial variation of the backlight unit and its correlated color temperature (CCT). Note that the final FPD products in practice cannot have perfectly uniform illumination and a consistent 6500 K of CIE D65 illuminant over the entire screen. Therefore, most manufacturers in the FPD industry tolerate a certain variation of illumination and CCT per model. In this experiment, we chose one of the target products as a reference device, verified by a professional human assessor.

D. Mapping Colors into an Image Appearance Model

It is well known that a perceived color difference is affected by its spatial frequency [27], i.e., a medium-sized color defect can be easily detected by a human assessor, whereas a small color defect is less perceivable. To account for the contrast sensitivity of the human eye, an image appearance model proposed in a visual color difference predictor [26] is employed. Once the measurements of radiance are obtained in CIEXYZ coordinates from FPDs, the CIEXYZ values are mapped into the hue-linear color space, i.e., LAB2000HL [19]. Then, contrast sensitivity functions are applied to each LAB2000HL channel to predict the visual difference of color defects at various frequency levels. See Figure 3 for this computational workflow. Figure 3(c) shows the spatial filters that we employed:

$$\begin{aligned} \text{csf}_{\text{lum}}(f) &= a \cdot f^c \cdot e^{-b \cdot f}, \\ \text{csf}_{\text{chrom}}(f) &= a_1 \cdot e^{-b_1 \cdot f^{c_1}} + a_2 \cdot e^{-b_2 \cdot f^{c_2}}, \end{aligned} \quad (3)$$

where csf_{lum} is the contrast sensitivity function (CSF) for the luminance channel, and $\text{csf}_{\text{chrom}}$ is the CSF for the two color

Image appearance modeling

Evaluating color differences in the FPD

(a) Calibrated HDR radiance image in CIEXYZ (b) Hue-linear color coordinates (c) Applying contrast sensitivity functions (d) Evaluating color differences (d) Color difference map [ΔE_{HL}]
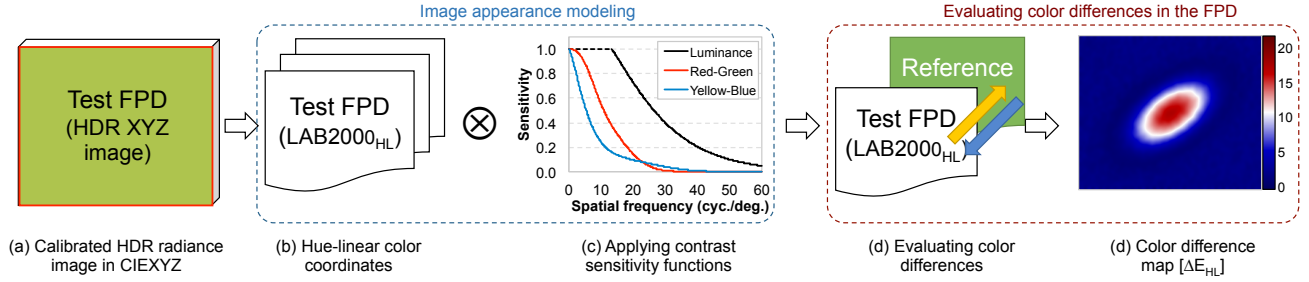
Fig. 3: Schematic diagram of our visual difference prediction workflow. (a) shows the calibrated HDR radiance image in CIEXYZ (see Section III-B). (b) indicates the hue-linear color space coordinates [19]. (c) These image coordinates are then convolved with three contrast sensitivity functions, respectively (Section III-D). (d) Finally, our workflow computes color differences between the test and the reference FPD (Section III-C), yielding a color difference map with perceptually uniform scales ΔE_{HL} (Section III-E).

opponent channels. The parameters a, b, and c in $\mathrm{csf}_{\mathrm{lum}}$ are set to 0.63, 0.085, and 0.616, and the parameters a_1, b_1, c_1, a_2, b_2, and c_2 in $\mathrm{csf}_{\mathrm{chrom}}$ are set to 91.228, 0.0003, 2.803, 74.907, 0.0038, and 2.601 for the red-green channel, and 5.623, 0.00001, 3.4066, 41.9363, 0.083, and 1.3684 for the blue-yellow channel in our experiments, following Lissner et al. [26]. In practice, these spatial filters are multiplied with each LAB2000HL channel after being converted to the frequency domain. The frequency property is computed as follows:

$$f = d \cdot cpd,$$
$$cpd = n \cdot \left(4 \tan^{-1}\left(\frac{0.5s}{wd}\right)\right)^{-1}, \tag{4}$$

where f is an input parameter in Equation (3); d is a pixel-wise distance from the center in the Fourier domain; and cpd indicates cycles-per-degree which can be calculated from the device specification. n is the number of pixels in an FPD along one side, and s is the physical length of the side in millimeters. Here, wd is the distance between the FPD and the camera in millimeters.

Note that these filters are low-pass filters that compress high frequency information at the different levels of each channel. These low-pass filters attenuate high frequencies which are below the visibility threshold while maintaining the mean intensity and preventing the unnatural exaggeration of certain frequencies.

E. Color Difference Map

After the spatial filters are applied for each channel, a color difference per pixel is calculated as an Euclidean distance value of ΔE_{HL} in the LAB2000HL color space with respect to the reference device. Note that this Euclidean distance in the LAB2000HL space ΔE_{HL} is designed to be equivalent to the standard color difference ΔE_{00} in the CIELAB space [19]:

$$\Delta E_{HL} = \sqrt{\Delta L_{HL}^{*}{}^2 + \Delta a_{HL}^{*}{}^2 + \Delta b_{HL}^{*}{}^2}, \tag{5}$$

where $\Delta L_{HL}^* = L_{HL_1}^* - L_{HL_2}^*$, $\Delta a_{HL}^* = a_{HL_1}^* - a_{HL_2}^*$, $\Delta b_{HL}^* = b_{HL_1}^* - b_{HL_2}^*$. Here L_{HL}^*, a_{HL}^* and b_{HL}^* denote the achromatic and color opponent channels in the LAB2000HL space. Finally, filtering of the difference map with a threshold level yields a binary map that indicates the color defect region in the FPD.
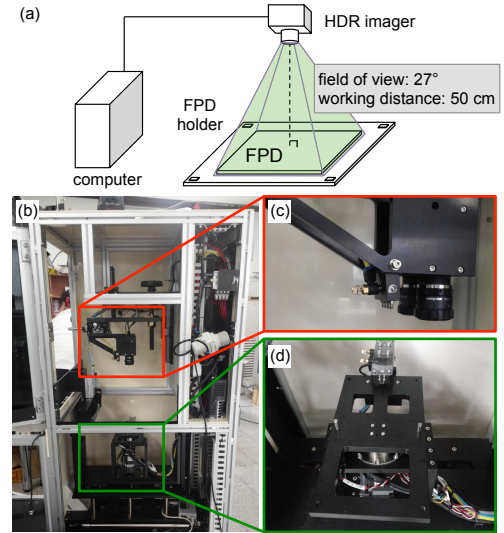

Fig. 4: (a) Diagram of our system, consisting of an HDR imager, a mobile FPD holder and a computer. (b) The inside of our system. (c) Two cameras, and (d) FPD holder for a mobile display panel.

IV. EXPERIMENTAL SETUP

Several experiments were conducted to validate the performance of our framework. It was implemented with a 5.0MP giga-ethernet camera (PointGrey Grasshopper2) with a 35 mm lens mounted. The imaging sensor in the camera was Sony ICX625, of which the sensor format is 2/3" and its pixel pitch is 3.45 μm. The aperture of the lens was set to $f/8$, allowing us to secure a depth of field sufficient to handle the thickness variation of display products. Four-inch IPS LCD panels were tested, of which the pixel resolution was 480×800 in a series of mobile phones. The pixel density of the LCD panel under test is 233 dots-per-inch with a pixel pitch of 109 μm. In order to diverse color defect examples, various synthetic color defects were also generated in addition to the actual color defects.

For HDR imaging, four LDR images were captured with incremental exposure time of 32, 64, 128, and 256 milliseconds. The sensor gain was set to 0 dB. As shown in Figure 4, the camera was installed at a distance of 50 cm. The centers of the sensor and the FPD were aligned perpendicularly along its optical axis to reduce moiré artifacts over the captured images.

(a) Measurement uncertainty

	Spectroradiometer				HDR imager			
	D65	D50	A	FPD	D65	D50	A	FPD
u	0.1942	0.2066	0.2592	0.1928	0.2026	0.2119	0.2771	0.1924
v	0.3105	0.3254	0.3520	0.3061	0.2985	0.3110	0.3455	0.3060
CCT [K]	6915	5151	2769	7496	7715	5713	2452	7550
$u_c(u)$	0.00004	0.00005	0.00005	0.00004	0.00017	0.00018	0.00021	0.00016
$u_c(v)$	0.00003	0.00003	0.00001	0.00004	0.00023	0.00022	0.00015	0.00025
$u_c(CCT)$ [K]	4.1	2.5	1.2	5.5	31.9	16.6	3.5	31.0

(b) Measurement accuracy

	Training	Test
ΔXYZ	1.902	5.748
Δuv	0.0010	0.0008
Δu	0.0005	0.0006
Δv	0.0004	0.0006
ΔCCT	12.3	25.1
ΔE_{00}	0.513	0.377
ΔE_{HL}	0.186	0.213

TABLE I: (a) compares measurement uncertainty of a reference spectroradiometer and our HDR imaging system under four different illuminants, three different types of CIE Illuminants and an FPD device. The first three rows present CIE uv and CCT measurements under each illuminant. The following three rows show the measurement uncertainties of each property, computed by the Gardner's method. (b) shows the measurement accuracy of our system. It is evaluated by computing median differences of colors measured by the spectroradiometer and our system in terms of CIE XYZ, CIE uv, CCT, CIE ΔE_{00}, and ΔE_{HL}.

V. RESULTS

A. Measurement Uncertainty

The measurement accuracy of the reference spectroradiometer and our HDR imaging system is validated by evaluating uncertainty, following Gardner [28], [29], based on an ISO standard for uncertainty propagation. As the measurement uncertainty of an imaging system varies upon the spectral power distribution of a light source, we evaluated the performance in three different types of CIE Illuminants (D65, D50 and CIE Illuminant A) and the FPD device illuminant. For the standard illuminations, we used a calibrated illumination booth, PANTONE Color Viewing Light (PVL-511).

Table I(a) presents the evaluated uncertainties in terms of CIE uv and CCT. The reference spectroradiometer shows a lowest uncertainty with a type of CIE Illuminant A, whereas the uncertainty increases when the CCT increases ($u_c(u) = u_c(v) = 0.00004, u_c(CCT) = 5.5\,K$ for FPD). Our HDR imaging system shows a similar trend in measurement uncertainty. The uncertainty of our system is also lowest with CIE Illuminant A. The uncertainty of the system also increases when the temperature rises ($u_c(u) = 0.00016, u_c(v) = 0.00025, u_c(CCT) = 31.0\,K$ for FPD). Although the uncertainty varies depending on CCT, our HDR imaging system performs consistently even under high color temperatures of the FPD devices.

Since we evaluate the measurement uncertainty of the reference and our system, we then validate the measurement accuracy that describes measurement differences in both instruments, shown in Table I(b). We first captured a series of colors displayed in a FPD using both instruments, we then calculate the differences of colors measured by the two instruments. The training set, shown in Figure 2 (left bottom), consists of 24 color patches, which are used to calibrate our system. The test set consists of new nine colors that range from blue to orange, representing the color variation of blackbody radiation. Each row in Table I(b) shows median errors in terms of CIE XYZ, CIE uv, CCT, CIE ΔE_{00} and ΔE_{HL}. Our system agrees with the reference measurements consistently with training and test color samples.

B. Detecting a Color Defected Region

Once a display image is captured and converted to the LAB2000HL space, color differences ΔE_{HL} are computed
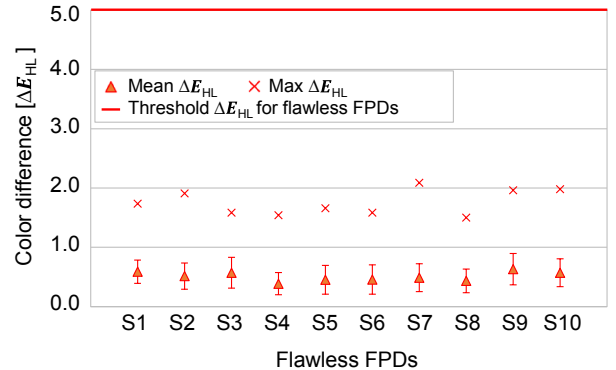

Fig. 5: The spatial variation of ten flawless FPDs were evaluated as the mean ΔE_{HL} values. The measured mean values were around 0.5096 with standard deviation 0.2287. The measured maximum differences were below than 2.3550. The color defect threshold was determined as 5.0, making allowances for the maximum color difference and measurement uncertainty.
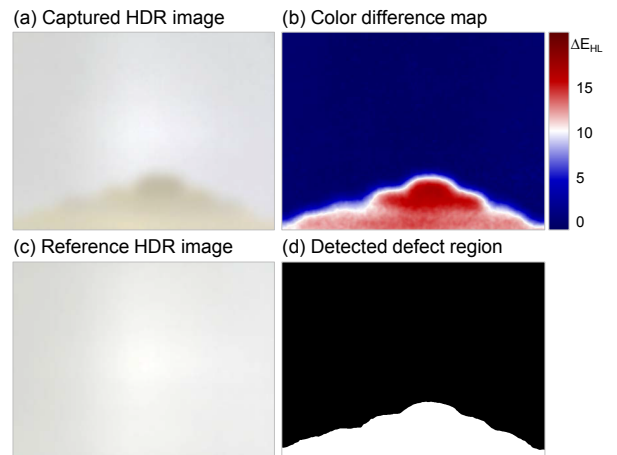

Fig. 6: Illustration of color defect detection using a reference image and a color difference map. (a) a captured HDR image with a yellow defect on the long edge. (b) color difference map that show the perceptual color difference between (a) and (c). (c) a reference image of a flawless display. (d) a binary image obtained by setting a threshold 5.0 in (b).

per pixel in the image with regard to the reference image. We then test if the ΔE_{HL} values are higher than a threshold to find out color defect regions in the device. Note that we sampled ten flawless displays to determine the threshold level for the reference display. Figure 5 presents the averaged ΔE_{HL} values of the ten devices as 0.5096 with standard deviation of 0.2287. The maximum differences in the displays are below than 2.3550. Consequently the threshold for color defects was set to ΔE_{HL} 5.0, making allowances for the maximum color difference of flawless displays and the uncertainty of our system.

Testing color differences with the threshold yields a binary image that indicates defect regions in an FPD. Figure 6 shows an example color difference map of an FPD with a yellowish color defect. The color difference map (b) reflects the perceptual difference between the test image (a) and the reference image (c). The defect region can be clearly filtered out in the binary image (d) by setting a threshold.

C. Accuracy Comparison

Figure 7 compares the accuracy performance of various defect detection algorithms for various types of defects: SEMI JND [13] (b), Fan & Chuang [8] (c), Gan & Zhao [9] (d), and our method (e). Each method is compared with the defected area inspected by a human assessor (f). The numbers shown are the overlap scores as percentage, defined as $s = (a_1 \cap a_2)/(a_1 \cup a_2) \times 100$ [%], where a_1 is the area detected by each method, a_2 is the human assessor's detection area, and $\cap/\cup$ represents the intersection/union area of the two regions. For SEMI JND (b), the SEMU index in the SEMI document is directly applied in the luminance channel. The luminance contrast was calculated by subtracting the test image from the reference image.

The SEMI JND method can detect the achromatic mura well (first row), and some of severe color defects that cause significant luminance variation (last two rows). Fan & Chuang's method (c) yielded results similar to those obtained by SEMI JND (b). However, as methods (b) and (c) are designed to detect luminance variation in FPDs, they are not able to detect subtle color defects (second to fourth rows). For the active contour method of Gan & Zhao (d), the input parameters are adjusted to best detect the achromatic mura in the first row. This method can also detect the subtle boundaries of color defects in all cases. However, their method fails to determine the defected area accurately with a single parameter. To determine the correct region for each input, their method requires adjustment of the operating parameters. In contrast, our method performs consistently without parameter adjustment. Column (e) shows our results which are very similar to human assessor's.

D. Time Performance Comparison

The average running times of the methods are tabulated in Table II. The long running time of Gan & Zhao method is mainly due to the large input image (980×760) and large number of iterations (200 times). The main bottleneck of our method is the forward/inverse Fourier transformation for bandpass filtering in the image appearance model. Although our method takes a longer time than other luminance-based methods, such as SEMI JND and that of Fan & Chuang, it can

Methods	SEMI JND	Fan & Chuang (2010)	Gan & Zhao (2013)	Our method
CPU times	0.76 s	0.22 s	233.27 s	2.07 s

TABLE II: Time performance comparison. CPU running times are averaged for seven input images. Although the proposed method takes longer than other luminance-based mura detection methods, it can robustly detect subtle color defects.

robustly measure subtle color defects that otherwise were unable to be detected (see Figure 7). All methods were implemented in MATLAB for a fair comparison.

VI. DISCUSSION

In the implementation of this proposed framework, several practical issues arose that remain as subject of future work. This section shares the experiences which could be useful for those who may apply this framework in manufacturing process.

While capturing a FPD with a camera, a moiré pattern appeared as a high-frequency spatial artifact. This type of artifact was avoided using a low-pass filter approach in the image appearance model. As mentioned in Sec. III-D, the hue-linear color coordinates in luminance and two color opponents were filtered with three different low-pass filters respectively. Hence, the image measurements of our workflow did not have to deal with the problem of moiré artifacts. Note that this low-pass filtering process degrades the performance in inspecting small defects such as a dead pixel in FPDs. The implemented system includes an additional monochromatic camera to detect defective pixels exclusively.

The CCTs of the FPD panels under test varied considerably in this experiment with a standard deviation of 379 K. Most panel manufacturers have their own standards for the target CCT and variation for classifying flawless displays. For example, the ANSI standard for solid state lighting products defines the standard color temperature as 6500 K ± 500 K. Therefore, in the experiment, the overall CCT of panels was tested first, following the manufacturer's CCT standard to filter out defective panels. Then, our method was applied to detect local color defects using the image-appearance modeling approach. Note that the reference white parameter in the image appearance model was determined by calculating the average pixel values in the brightest area. This implies that the human eye chromatically adapts to display media while they are looking at a device.

VII. CONCLUSION

This paper presented a color measurement framework for FPD panels using HDR imaging and image appearance modeling. Our framework extends the previous luminance-based inspection framework to the perceptually uniform color domain via physically meaningful HDR imaging. It was shown that our framework is able to detect color defects in FPDs that are undetectable with the previous approaches. It was also demonstrated that this proposed framework agrees with the current mura standard, SEMI JND [13]. The experimental results validate the performance of this framework in detecting defects in arbitrary type, color, size, position, and shape. Integration of this proposed method is expected to enhance the production quality of FPDs at a relatively low additional cost.
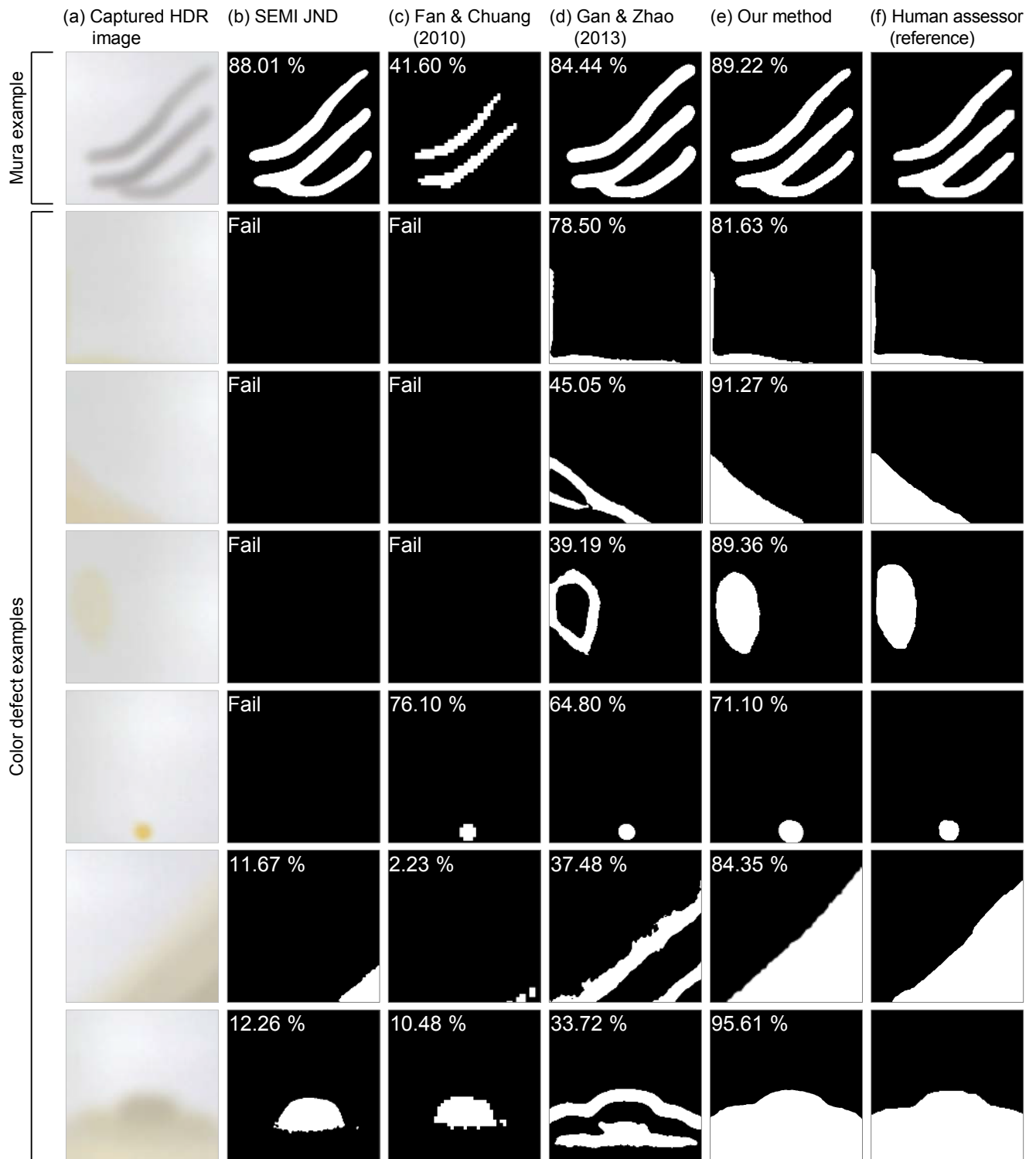
Fig. 7: Accuracy comparison of our method (e) with existing mura detection algorithms (c) and (d) as well as mura standard (b). Each method is compared to a human assessor's work (f), and the overlap of detected defect region w.r.t. the human assessor's is shown as a percentage. (a) shows the captured HDR images of the tested FPDs. (b) and (c) successfully detect the dark mura (first row), but they are incapable of detecting subtle color defects (second to fourth row). (d) detects subtle boundaries in all cases, but the detected area does not agree well with the human assessor's. (e) detects the same defect region, virtually identical to the human assessor's perception (f).

REFERENCES

[1] S. Shirmohammadi and A. Ferrero, "Camera as the instrument: the rising trend of vision based measurement," *IEEE Instrum. Meas. Mag.*, vol. 17, no. 3, pp. 41–47, 2014.

[2] F. Adamo, F. Attivissimo, and A. Di Nisio, "Calibration of an inspection system for online quality control of satin glass," *IEEE Trans. Instrum. Meas.*, vol. 59, no. 5, pp. 1035–1046, 2010.

[3] R. Anchini, G. Di Leo, C. Liguori, and A. Paolillo, "Metrological characterization of a vision-based measurement system for the online inspection of automotive rubber profile," *IEEE Trans. Instrum. Meas.*, vol. 58, no. 1, pp. 4–13, 2009.

[4] Y. Li, Y. F. Li, Q. L. Wang, D. Xu, and M. Tan, "Measurement and defect detection of the weld bead based on online vision inspection," *IEEE Trans. Instrum. Meas.*, vol. 59, no. 7, pp. 1841–1849, 2010.

[5] J. Z. Tsai, R.-S. Chang, and T.-Y. Li, "Detection of gap mura in TFT LCDs by the interference pattern and image sensing method," *IEEE Trans. Instrum. Meas.*, vol. 62, no. 11, pp. 3087–3092, 2013.

[6] X. Bi, C. Zhuang, and H. Ding, "A new mura defect inspection way for TFT-LCD using level set method," *IEEE Signal Process. Lett.*, vol. 16, no. 4, pp. 311–314, 2009.

[7] L.-C. Chen and C.-C. Kuo, "Automatic TFT-LCD mura defect inspection using discrete cosine transform-based background filtering and just noticeable difference quantification strategies," *Meas. Sci. Technol.*, vol. 19, no. 1, p. 015507, 2008.

[8] S.-K. S. Fan and Y.-C. Chuang, "Automatic detection of mura defect in TFT-LCD based on regression diagnostics," *Pattern Recogn. Lett.*, vol. 31, no. 15, pp. 2397–2404, 2010.

[9] Y. Gan and Q. Zhao, "An effective defect inspection method for LCD using active contour model," *IEEE Trans. Instrum. Meas.*, vol. 62, no. 9, pp. 2438–2445, 2013.

[10] A. B. Watson, "The spatial standard observer: A human vision model for display inspection," in *SID Symp. Dig. Tec. Papers*, vol. 37, no. 1. Wiley Online Library, 2006, pp. 1312–1315.

[11] M. H. Kim, T. Weyrich, and J. Kautz, "Modeling human color perception under extended luminance levels," *ACM Trans. Graph.*, vol. 28, no. 3, pp. 27:1–9, 2009.

[12] M. H. Kim, T. Ritschel, and J. Kautz, "Edge-aware color appearance," *ACM Trans. Graph.*, vol. 30, no. 2, pp. 13:1–9, 2011.

[13] Semiconductor Equipment and Materials International (SEMI), "Definition of measurement index (SEMU) for luminance Mura in FPD image quality inspection," 2002.

[14] H. Kostal, G. Pedeville, and R. Rykowski, "Methods for measuring display defects as correlated to human perception," in *IS&T/SPIE Electron. Imag.*, 2009, pp. 72420G:1–9.

[15] H. I. Son, "Automatic inspection method for macro defects in TFT-LCD color filter fabrication process," *IEICE Electron. Express*, vol. 6, no. 8, pp. 516–521, 2009.

[16] T. Asano, K. Kawame, J. Mochizuki, and N. Fukuhara, "Automated color inspection system for color CRT displays," in *Int. Conf. Ind. Electron., Control, Instrum. Autom.* IEEE, 1992, pp. 725–730.

[17] T. Asano, T. Kondo, and S. Maeda, "Mura grade evaluation based on S-CIELAB color system," in *SID Symposium Digest of Technical Papers*, vol. 45, no. 1. Wiley Online Library, 2014, pp. 1081–1084.

[18] X. Zhang and B. Wandell, "A spatial extension of CIELAB for digital color-image reproduction," *J. Soc. Inf. Display*, vol. 5, no. 1, pp. 61–63, 1997.

[19] I. Lissner and P. Urban, "Toward a unified color space for perception-based image processing," *IEEE Trans. Image Process.*, vol. 21, no. 3, pp. 1153–1168, 2012.

[20] A. R. Várkonyi-Kóczy and A. Rovid, "High-dynamic-range image reproduction methods," *IEEE Trans. Instrum. Meas.*, vol. 56, no. 4, pp. 1465–1472, 2007.

[21] A. R. Várkonyi-Kóczy, A. Rovidz, and T. Hashimoto, "Gradient-based synthesized multiple exposure time color HDR image," *IEEE Trans. Instrum. Meas.*, vol. 57, no. 8, pp. 1779–1785, 2008.

[22] V. Z. Groza, "High-resolution floating-point ADC," *IEEE Trans. Instrum. Meas.*, vol. 50, no. 6, pp. 1822–1829, 2001.

[23] M. H. Kim and J. Kautz, "Characterization for high dynamic range imaging," *Comput. Graph. Forum*, vol. 27, no. 2, pp. 691–697, 2008.

[24] M. D. Fairchild and G. M. Johnson, "iCAM framework for image appearance, differences, and quality," *J. Electron. Imag.*, vol. 13, no. 1, pp. 126–138, 2004.

[25] Z. Wang, A. C. Bovik, H. R. Sheikh, and E. P. Simoncelli, "Image quality assessment: from error visibility to structural similarity," *IEEE Trans. Image Process.*, vol. 13, no. 4, pp. 600–612, 2004.

[26] I. Lissner, J. Preiss, P. Urban, M. S. Lichtenauer, and P. Zolliker, "Image-difference prediction: From grayscale to color," *IEEE Trans. Image Process.*, vol. 22, no. 2, pp. 435–446, 2013.

[27] P. G. Barten, *Contrast sensitivity of the human eye and its effects on image quality.* SPIE Press, Washington, 1999, ch. 8, pp. 27–66.

[28] J. L. Gardner, "Uncertainty estimation in colour measurement," *Color Res. Appl.*, vol. 25, no. 5, pp. 349–355, 2000.

[29] J. Gardner, "Correlated colour temperature-uncertainty and estimation," *Metrologia*, vol. 37, no. 5, p. 381, 2000.
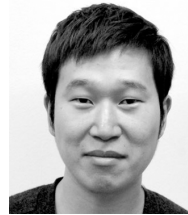
Giljoo Nam is a PhD student in the KAIST Visual Computing Laboratory. He received his master degree in computer science from KAIST in 2014. Prior to KAIST, he received a bachelor degree in electronic engineering from Korea University in 2012. His research interests include imaging spectroscopy and 3D scanning. **Address:** Giljoo Nam, KAIST School of Computing, 291 Daehak-ro, Yuseong-gu, Daejeon, 305-701, South Korea, gjnam@vclab.kaist.ac.kr
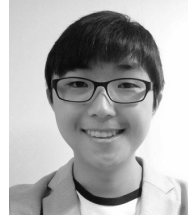
Haebom Lee is an MS student in KAIST Visual Computing Laboratory (VCLAB). Prior to KAIST VCLAB, he received a bachelor degree in computer science from KAIST in 2009. His research focuses on building hyperspectral imaging systems. **Address:** Haebom Lee, KAIST School of Computing, 291 Daehak-ro, Yuseong-gu, Daejeon, 305-701, South Korea, hblee@vclab.kaist.ac.kr

Sungsoo Oh is a chief research engineer in the Production Engineering Research Institute of LG Electronics. He received a bachelor degree in electronic engineering from Hanyang University in 1998. His research interests include RF measurement algorithm of mobile communication, wireless connectivity and vision inspection. **Address:** Sungsoo Oh, Production Engineering Research Institute, LG Electronics, 222 LG-ro, Jinwi-myen, Pyeongtaek-si, Gyeonggi-do, 451-713, South Korea, sungsoo.oh@lge.com

Min H. Kim is an assistant professor of computer science at KAIST, leading Visual Computing Laboratory. Prior to KAIST, he worked as a postdoctoral researcher at Yale University. He received his PhD in computer science from University College London (UCL) in 2010. His research interests include color, 3D imaging and visual perception. **Address:** Min H. Kim, KAIST School of Computing, 291 Daehak-ro, Yuseong-gu, Daejeon, 305-701, South Korea, minhkim@vclab.kaist.ac.kr